# Stall Behavior Curved Planform Wing Analysis with Low Reynolds Number on Aerodynamic Performances of Wing Airfoil Eppler 562

*Setyo Hariyadi S.P.[*], Bambang Junipitoyo*
*Department of Aircraft Engineering, Politeknik Penerbangan Surabaya,*
*Human Resources Development Agency of Transportation,*
*Ministry of Transportation, Republic of Indonesia,*
*Jemur Andayani I/73 Wonocolo Surabaya 60236 Indonesia*
** setyo_hariyadi@poltekbangsby.ac.id*

*Sutardi, Wawan Aries Widodo*
*Department of Mechanical Engineering,*
*Faculty of Industrial Technology and Systems Engineering,*
*Institut Teknologi Sepuluh Nopember, Jl. Arief Rahman Hakim,*
*Surabaya 60111 Indonesia*

ABSTRACT

*On airplanes and UAVs, a stall is something that is always attempted to avoid. Stalling can also be aided by the employment of planform wings with varying geometry. Curved wing variations are often used in UAV applications, especially at low Reynolds numbers. This study discusses stall behavior on rectangular, elliptical, semi-elliptical, and Schuemann wings. Numerical simulations were performed using the turbulent k-ω SST model using Ansys Fluent 19.1. The airfoil used in this study was Eppler 562 at Reynolds number 2.34 x $10^4$. The angles of attack observed were $0^o$, $2^o$, $4^o$, $6^o$, $8^o$, $10^o$,$12^o$, $15^o$, $17^o$, $19^o$, and $20^o$. The Schuemann wing has the best performance that is indicated by the delaying of the stall point, which is at an angle of attack $\alpha = 15^o$, while the rectangular wing produces the highest lift to drag ratio compared to other planform wings. The confluence of the main flow and backflow forms towards the mid-span as the angle of attack increases. The rectangular wing produces high vorticity in the wingtip area due to the tip-*

ISSN 1823-5514, eISSN 2550-164X
Received for review: 2021-07-01
Accepted for publication: 2021-10-03
Published: 2022-01-15

*vortex phenomenon, while the elliptical and Schuemann wing in the leading edge area due to the geometry of the leading edge.*

**Keywords:** *Planform Wing; Airfoil; Eppler 562; Stall Behaviour; UAV*

## Nomenclature

| | |
|---|---|
| $c_d$ | Profile Drag Coefficient |
| $D_f$ | Skin Friction Drag |
| $q_\infty$ | Dynamic Pressure |
| S or l | Wingspan |
| $D_P$ | Pressure Drag |
| $C_{Di}$ | Induced Drag Coefficient |
| $C_D$ | Total Drag Coefficient |
| $C_{Df}$ | Skin Friction Drag Coefficient |
| $C_{DP}$ | Pressure Drag Coefficient |
| e | span efficiency or Oswald's factor or Oswald's span efficiency factor |
| AR | Aspect Ratio |
| $y^+$ | A non-dimensional distance (based on local cell fluid velocity) from the wall to the first mesh node |
| α | Angle of Attack |
| Re | Reynolds number |
| $C_L$/ $C_D$ | Lift Coefficient/ Drag Coefficient, Lift to Drag Ratio |
| $C_L$ | lift coefficient |
| C | chord line |

## Introduction

A stall is an event where the airfoil loses lift suddenly as the angle of attack increases. Stall begins with the occurrence of separation where the fluid flow begins to leave the surface of the airfoil. The separation progresses as the angle of attack increases, causing the fluid flow to dramatically depart the airfoil surface. When massive separation occurs, the lift will suddenly decrease drastically. This event occurs at a critical angle of attack and depends on many factors, including the type of airfoil, Reynolds number, type of fluid used, wing planform, and others.

The separation that occurs at low and high Reynolds numbers is very different. At a high Reynolds number, the flow momentum is greater so it tends to attach back to the surface of the airfoil. Likewise, the phenomenon of airplanes is very different from unmanned aerial vehicles. In addition to being

caused by each operating at different Reynolds numbers, aircraft also have an airspeed indicator so that the tendency for a critical angle of attack to occur can be avoided. In unmanned aerial vehicles, generally, there is no airspeed indicator, so you have to estimate through the lift coefficient graph of the type of wing airfoil used [1].

Generally, the separation starts from the trailing edge area but does not rule out the possibility that the separation starts from the leading edge. This is caused by bubble separation that arises due to surface roughness. Generally, the separation that occurs at the leading edge will be attached back to the surface of the wing. The separation phenomenon at the leading edge can be more clearly seen in the tin airfoil which shows its evolution in more detail. Separation can also occur in the wing root area where there is a junction between the wing and the fuselage wall surface. The separation in this area is caused by the angle of attack and the geometry between the wing and fuselage [2,3].

Several researchers have identified a variety of additional sorts of stalls while looking at the occurrence process. Dynamic stall is often said to occur in helicopter rotors [4,5]. However, some experts often mention that dynamic stall occurs when the aircraft moves suddenly, causing a sudden high angle of attack. This movement usually occurs due to aircraft maneuvers that cause a combination of yawing, rolling, and pitching movements [6]–[8]. Each movement caused by a sudden change in the angle of attack exhibits a different flow structure. At each angle of attack in addition to showing a different structure and flow pattern, it also produces a drag coefficient, lift coefficient, and pressure coefficient that changes drastically. Other researchers also mention the tip stall that occurs on the swept planform and tapered wing. [9]–[11]. In the swept-wing planform, the center of gravity position is located in front of the wing so that it must be balanced by the wing behind it. In general, the leading edge of the swept-wing planform has a maximum coefficient of lift and a faster stall point than the shoulder airfoil and trailing edge. This is also caused by the tip vortex and downwash on the side of the wingtip. Shevell [12] added another dangerous stall type, which is often referred to as a deep stall. Deep stalls occur on aircraft with a T-tail configuration and a rear-mounted engine. On the T-tail, the turbulent wake of the wing, engine nacelle, and fuselage covers the horizontal and vertical stabilizer so that the elevator does not function effectively, resulting in a stall [13,14].

In the world of aviation, when a stall occurs, all primary control surfaces on the aircraft (aileron, elevator, rudder) do not function perfectly. It depends on how the planform of the wings is. The wing planform will determine the angle of twist of the aircraft's movement to avoid decreasing the effectiveness of the ailerons during a stall so that the aircraft can still be controlled even if a stall occurs. However, in aerobatic aircraft and fighter aircraft, the stall is used for braking in extreme maneuvers. Under certain

conditions, the stall will evolve into spin motion. In the spin condition, one wing stalls, and the other wing still maintains its flight or both of them are stalled but at different angles of attack, resulting in a rotating motion [1].

The use of unmanned aerial vehicles (UAV) generally does not have an airspeed indicator so that it cannot indicate a stall warning as on an airplane. UAV maneuvers that cause a combination of yawing, rolling, and pitching movements cannot be controlled perfectly so that the wings accidentally create extreme angles of attack that suddenly cause dynamic stalls. This is supported by the speed of the UAV which tends to use a low Reynolds number [15, 16] and a low altitude which increases the tendency for accidents to occur. Therefore, in this study, we will discuss the pattern of stalls with a low Reynolds number to clarify stall behavior in maneuvering the use of UAVs.

The outputs of this numerical simulation study include aerodynamic performance (drag, lift, lift to drag ratio), three-dimensional flow patterns on the upper surface, pressure coefficient contours, and vorticity magnitude contours on the x-axis. With this output, it shows the characteristics and forms of stall behavior and the influence of wing geometry. The effects of aerodynamic performance (drag, lift, lift to drag ratio), three-dimensional flow patterns on the upper surface, pressure coefficient contours, and vorticity magnitude contours are discussed in the discussion section.

## Methods

### Mathematical model

One of the purposes of using an elliptical wing is to have a minimum load distribution and induced drag. In the subsonic finite wing, the total drag is the sum of the induced drag, skin friction drag, and pressure drag. According to Anderson [17]. In the moderate angle of attack, the definition of profile drag, induced drag, total drag, and lift to drag ratio are:

$$c_d = \frac{D_f + D_{DP}}{q_\infty S} \tag{1}$$

$$C_{D,i} = \frac{D_i}{q_\infty S} \tag{2}$$

$$C_{D,i} = \frac{C_L^2}{\pi e AR} \tag{3}$$

$$C_D = c_d + C_{D,i} \tag{4}$$

$$Lift\ to\ Drag\ Ratio = \frac{C_L}{C_D} \quad (5)$$

## Numerical set-up

This research uses Ansys 19.1 software where Unsteady Reynolds Averaged Navier-Stokes (URANS) are based on finite volume. The turbulent model used is K-ω SST [18] which can capture a wide vortex structure with good accuracy [9,19]. The grid and meshing used have gone through independence where the chosen one uses $y^+<1$ [20] and the $C_D$ difference between each type of mesh is less than 0.02 [17]. The simulation domain uses the scheme used by Mulvany [21] by extending the side behind the wing by 7 times the chord line to clearly show the resulting vorticity. Table 1 shows the numerical setup of the research model. Figure 1 shows the research domain and in Figure 2 the research model is used. The use of the planform wing is based on Dole [1] and Gudmundsson [2].

Table 1: Description of research model

| Properties | Description |
|---|---|
| Model | 3D, Unsteady/Transient<br>Rectangular Wing<br>Elliptical Wing<br>Semi Elliptical Wing<br>Schuemann Wing |
| Airfoil | Eppler 562 |
| Fluids Properties | Density 1.225 kg/m3<br>Viscosity 0.000017894 kg/m-s |
| Boundary condition | Wing Wall<br>Outlet Outflow<br>Inlet Velocity Inlet<br>Wall Wall |
| Reynolds Number | Re = 2,34 x $10^4$ |
| Angle of Attack | $0^o$, $2^o$, $4^o$, $6^o$, $8^o$, $10^o$,$12^o$, $15^o$, $17^o$, $19^o$, and $20^o$ |

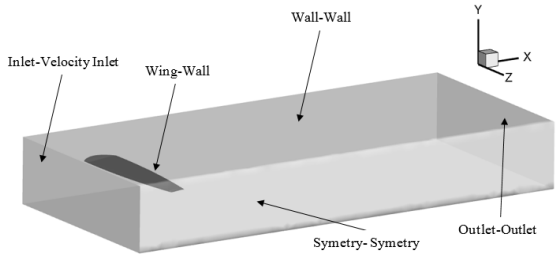


Figure 1: 3D Airfoil modeling domain with inflation layer on design geometry [21].

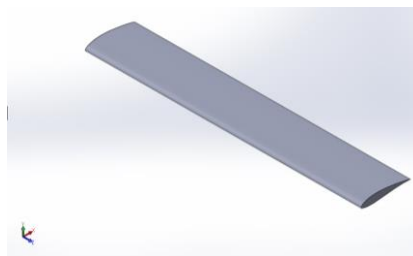

(a)

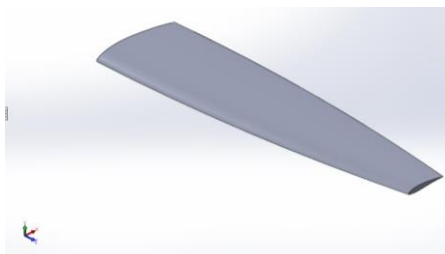

(b)

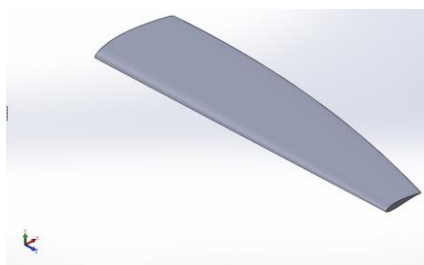

(c)

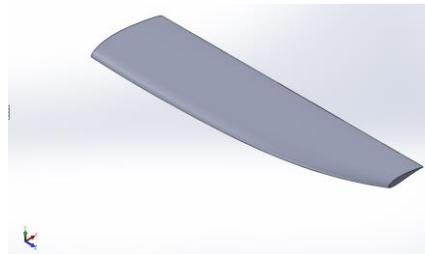

(d)

Figure 2: Research model, (a) rectangular wing, (b) elliptical wing, (c) semi elliptical wing, and (d) Schuemann wing.

## Results

### Aerodynamic performances

The lift coefficient, drag coefficient, and lift-to-drag ratio must all be considered when evaluating the aerodynamic performance of a wing shape. It is expected to illustrate the degree of the wing shape's impact as it covers roughly the same region. Figures 3-7 show a comparison of the components of the drag coefficient to compare the effects of the wing shape. The components of the drag coefficient shown are pressure drag, friction drag, and induced drag. The focus of the drag observation is at $\alpha = 10^{o}$-$15^{o}$ where according to Turanoguz and Hariyadi [22]–[26] there is a stall on the E562 airfoil. Of course, the stall does not occur suddenly, but at these angles, the drag pressure is greatest before the stall occurs. All wing shapes have tend for pressure drag to increase as the angle of attack increases. The rectangular wing produces a lower pressure drag than other wing shapes. The Schuemann wing shows an increase in pressure drag even though there was a slight decrease in the angle of attack $\alpha = 15^{o}$. The pressure drag on the Elliptical wing shows an increase along with the increase in the angle of attack. The increase in the pressure drag value also looks significant at the angle of attack $\alpha = 10^{o}$-$15^{o}$. The same thing is shown in the semi-elliptical wing where the increase in pressure drag occurs quite significantly along with the increase in the angle of attack.

In the friction drag, as shown in Figure 4, the rectangular wing shows a much smaller value than the other wing planforms. Schuemann wing, elliptical wing, and semi-elliptical wing show the consistency of relatively the same value where the semi-elliptical wing shows the highest value. In Figure 5, a comparison of the induced drag of the planform wings is shown. The value of the induced drag is very dependent on the high and low lift coefficient of the wing planform. The higher the lift coefficient, the greater the induced drag. The elliptical wing has the smallest induced drag value compared to other wing

planforms. While the semi-elliptical wing shows the highest value compared to the others. At the angle of attack $\alpha = 10^o$ and $\alpha = 12^o$, the Schuemann wing shows a higher value than the rectangular wing. The rectangular wing shows a higher value than the Schuemann wing at an angle of attack $\alpha = 12^o$. The results of the total drag of the planform wing are shown in Figure 6 where the Schuemann and semi-elliptical wings have a higher total drag value than the rectangular and elliptical wings. This total drag is the sum of pressure drag, friction drag, and induced drag.

The lift coefficients ($C_L$) of the rectangular, Schuemann wing, elliptical, and semi-elliptical wings are shown in Figure 7. There are variances in the placement of the stall point as indicated in the figure. On the elliptical wing, a stall occurs at the angle of attack $\alpha = 10^o$. Stall Rectangular and semi-elliptical wing points occur at the angle of attack $\alpha = 12^o$. While the Schuemann wing, stall occurs at the angle of attack $\alpha = 15^o$. Figure 7 also shows that the rectangular wing has the lowest lift coefficient value compared to other planform wings. In the same figure, it is shown that the semi-elliptical wing produces the highest lift coefficient compared to other planform wings. The following figure shows the lift to drag ratio of all planform wings. From Figure 8, it is shown that the rectangular wing produces the highest lift to drag ratio compared to other planform wings.

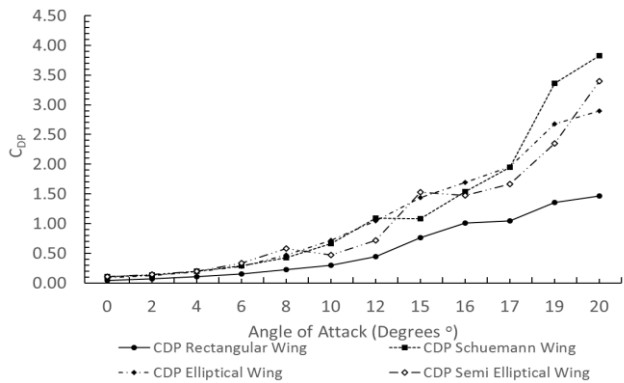


Figure 3: Comparison of the pressure drag coefficient of the model.

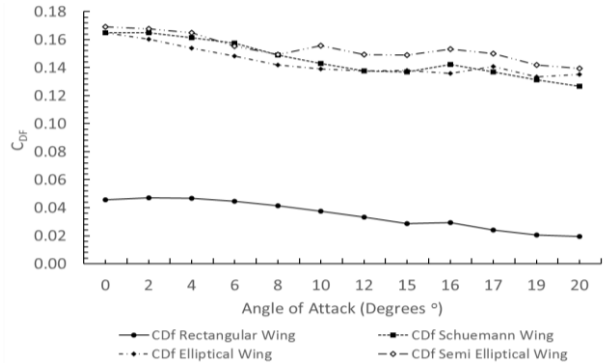


Figure 4: Comparison of the friction drag coefficient of the model.

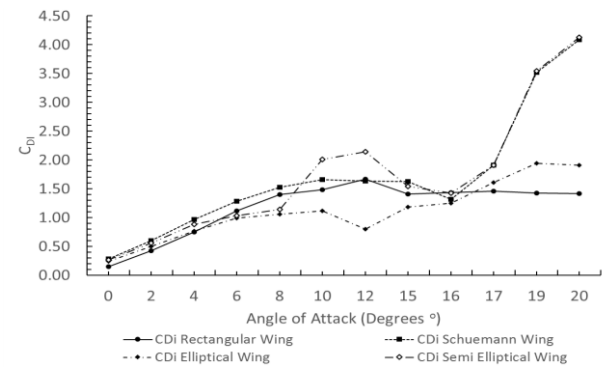


Figure 5: Comparison of the induced drag coefficient of the model.

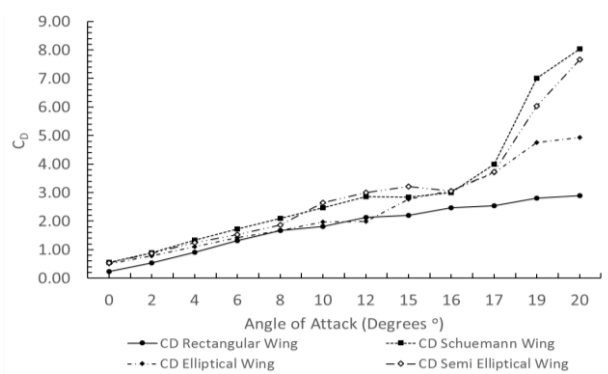


Figure 6: Comparison of the total drag coefficient of the model.

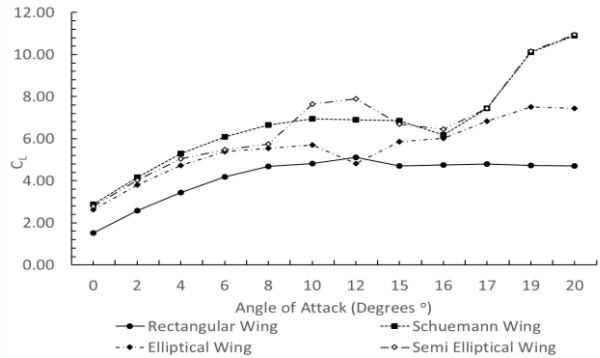


Figure 7: Comparison of the lift coefficient of the model.

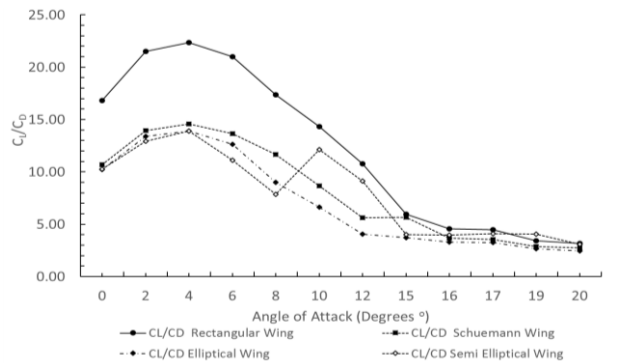


Figure 8: Comparison of the lift to drag ratio of the model.

## Three-dimensional flow patterns on the upper surface

Figure 9 shows the flow pattern on the upper surface in several wing shapes. The pressure contour on the surface of the wing shows that all configurations have undergone a separation, whose area almost reaches the leading edge. The area at the leading edge has lower pressure than the area behind it. On the rectangular wing $\alpha = 12^o$ it is shown that behind the low-pressure leading edge there is a concentration of secondary flow. The concentration of secondary flow, which is often referred to as focus, is due to the stronger backflow. In addition, the backflow that appears behind the leading edge causes a stronger separation. In the wingtip area, there is a confluence of areas from the leading edge and downstream which causes a stronger focus from the mid-span area. With an increase in the angle of attack, the backflow that arises is stronger and the focus that arises in the area behind the leading edge is increasing. This can be seen in the rectangular wing $\alpha = 15^o$.

On the elliptical wing $\alpha = 12^o$ it is shown that the focus is formed along the back of the low-pressure contour. This also shows that focus is the result of a confluence between the main flow and backflow along the wingspan. At some point in the wingspan, the focus is formed in areas that are close to the trailing edge. The elliptical wing $\alpha = 12^o$ shows that the low-pressure contour around the leading edge has a very narrow area. In the area around the wingtip, it is also shown that the jump of fluid flow from the lower side meets the backflow and main flow to produce a larger focus. As the angle of attack increases, the focus moves forward toward the leading edge. The confluence of the main flow, backflow, and flow from the lower side produce a stronger focus. This is shown on the elliptical wing $\alpha = 15^o$.

In the semi-elliptical wing $\alpha = 12^o$, it can be seen that the focus is formed as a confluence between main flow and backflow. Emerging focuses line up and side by side along the span. The jump of fluid flow from downstream meets the backflow after passing through the leading edge of the wingtip. The figure also shows that the pressure contour is relatively midway between the leading and trailing edges. With an increase in the angle of attack, the focus follows the pressure contour pattern which is progressively advancing towards the leading edge. Due to the influence of the fluid flow jump on the wingtip, the focus position moves slightly backward with increasing area. This pattern is shown on the semi-elliptical wing $\alpha = 15^o$.

On the Schuemann wing $\alpha = 12^o$, it can be seen that the intensity of the confluence between the main flow and backflow is decreasing compared to the other wing shapes. However, the focus pattern still follows behind the low-value pressure contour. On the wingtip side, backflow has reached the leading edge because it is influenced by the shape of the Schuemann wing. This is also influenced by the jump in fluid flow from the lower surface. As the angle of attack increases, the focus pattern increases in intensity to several places behind the leading edge.

## Pressure coefficient contour

Figure 10 shows the visualization of the pressure coefficient contour on the research wing form. Each wing form shows a different pressure coefficient pattern at the angle of attack $\alpha = 10^o$. On the rectangular wing $\alpha = 10^o$, it is shown that the pressure coefficient value -0.4 has reached the middle of the upper surface. Although the leading edge still has a low value, most of the upper surface has a relatively higher coefficient value. What needs to be noticed is that the contour with the same value has reached the middle of the upper surface and occurs from the wing root to the wingtip. This indicates that the separation has reached the middle of the upper surface. In this case, a severe separation leading to a stall has occurred or is about to occur. On the elliptical wing $\alpha = 10^o$, the pressure coefficient value -0.4 is not evenly distributed from the wing root to the wingtip as shown in the rectangular wing. However, it has

reached the middle of the upper surface. The pressure coefficient value of the leading edge is lower than that of the rectangular wing. The area with the same value is already as wide as the rectangular wing even though it has a lower value.

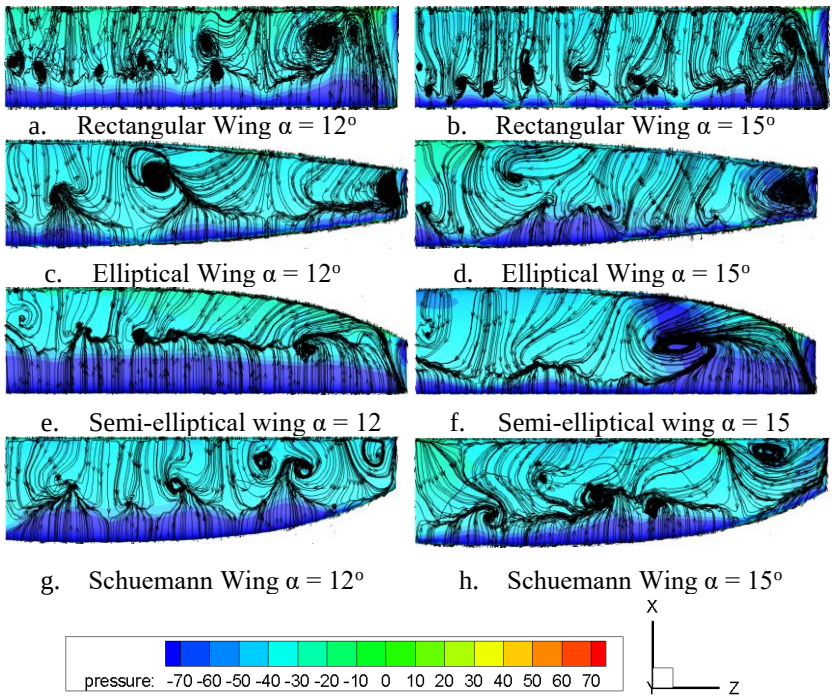


Figure 9: The pattern of the main flow and backflow along the wing span at Re = 2.34 x $10^4$.

In the semi-elliptical wing α = 10°, it is shown that starting from the leading edge the pressure coefficient value increases so that it reaches a little area behind the middle of the upper surface. The area behind the middle of the upper surface has a higher value and the pressure coefficient is relatively the same. The area with the same pressure value is evenly distributed from the wing root to the wingtip. The area with the same value is greater than the rectangular and elliptical wings. The geometry of the semi-elliptical wing greatly affects the area and the value of the pressure coefficient. This is shown in the area around the trailing edge which has the same value in most of the area. In the Schuemann wing α = 0°, where the geometric shape is the opposite of the semi-elliptical wing, it is shown that the leading edge has a lower

pressure coefficient value and gradually increases towards the middle of the upper surface. The area around the trailing edge shows that the area with the same pressure coefficient is evenly distributed from the wing root to the wingtip. However, the pressure coefficient value is lower than the semi-elliptical wing. This shows that the geometric shape of the Schuemann wing $\alpha = 10^o$ is very influential in reducing the pressure coefficient value in the trailing edge area.

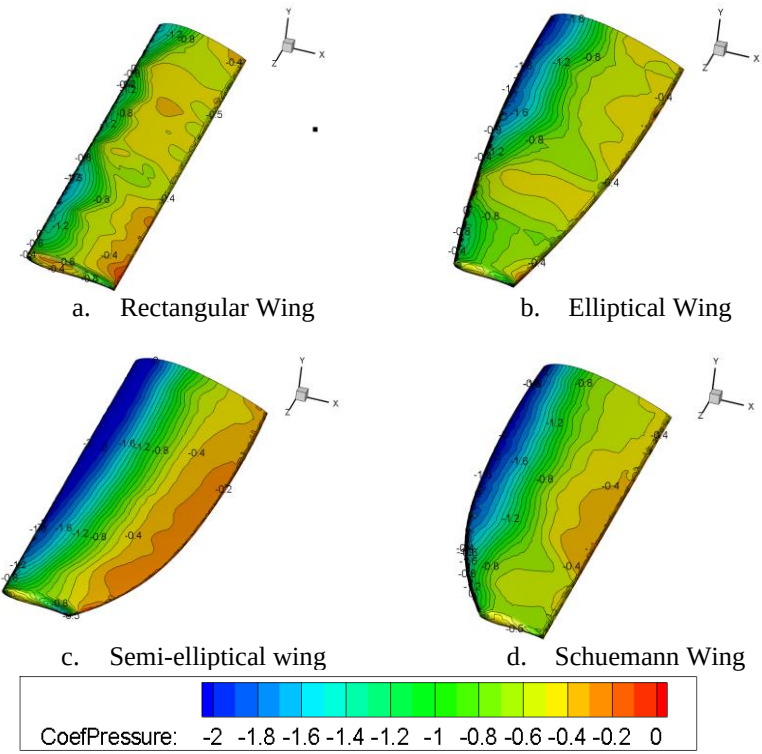


Figure 10: Contour of pressure coefficient along the wing span at $= 10^o$ with $Re = 2.34 \times 10^4$.

## Vorticity contour on the x-axis

Figure 11 shows the x-component of vorticity contour on the planform wing, rectangular, elliptical, semi-elliptical, and Schuemann wing at $\alpha = 12^o$. The rectangular wing shows that most of the vortices appear on the wingtip side. This is due to the tip vortex phenomenon in the area. The formation of the tip vortex starts from the tip of the leading edge on the wingtip which then moves towards the trailing edge. On the leading edge, it shows a small value because

it is not affected by the jump effect of fluid flow from the lower surface to the upper surface. Because the rotation is not right above the upper surface, the fluid flow jumps slightly backward. The vorticity appears to move slightly to the mid-span side of the trailing edge area because the jump in fluid flow has reached its highest value after starting from the leading edge.

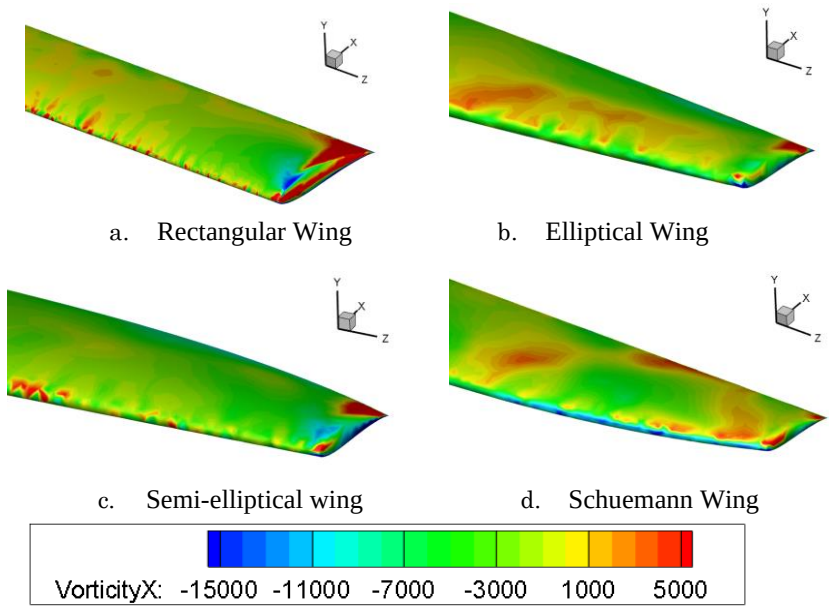


Figure 11: Vorticity contour on the x-axis along the wing span at = $12^o$ with Re = 2.34 x $10^4$.

In the elliptical wing, the x-component of vorticity increases slightly in the leading edge area and decreases in the trailing edge area. This is possible due to the influence of the geometry of the elliptical wing which is curved on the leading edge. On the wingtip side, the vorticity value also increased in the trailing edge area. The same thing happened to the semi-elliptical wing where there was an increase in the vorticity value on the trailing edge of the wingtip. However, due to the influence of the semi-elliptical wing geometry which is straight, there is no significant increase in the vorticity value on the leading edge. The influence of the geometry in the form of a curve can also be seen in the Schuemann Wing where the vorticity has increased in value at the leading edge on the mid-span and wingtip sides. In the trailing edge area, the value also increases which is connected to the leading edge. A flow may re-attach phenomenon occurs from the mid-span side towards the wingtip. At the end of

the trailing edge on the wingtip side, there is also a tip-vortex even though the area looks not so wide.

## Discussion

### Stall behaviour and flow pattern

The separation pattern or stall behaviour produced in this study is slightly different from that of Dole [1] and Gudmundsson [2]. The most important thing that distinguishes it is the freestream velocity used. Dole [1] and Gudmundsson [2] use freestream velocity on airplanes while in this study it is minimal freestream used in unmanned aerial vehicles (UAV). This is the main reason that the resulting separation pattern is different. As it is known that the altitude and velocity of airplanes and UAVs are different, these two things deserve special attention.

The confluence between the main flow and secondary flow on the upper surface shows a pattern that follows the pressure contour. This is especially true at the leading edge of the upper surface where the confluence between the main flow and secondary flow occurs right behind it. This happens at the angle of attack $\alpha = 12^{o}$. At the angle of attack $\alpha = 15^{o}$, the flow pattern tends to be irregular and does not have a certain pattern, this is influenced by other flows from the wingtip direction. The airflow from the wingtip direction produces a bigger, irregular vortex that does not follow the pressure contour pattern.

As the angle of attack increases, so does the size of the concentration that is created. Because the tip vortex on the trailing edge region is growing greater, the momentum from the wingtip side is also increasing bigger, the attention shifts to the mid-span on the wingtip side. This can be seen in rectangular, elliptical, and semi-elliptical wings. In the Schuemann wing, the focus that occurs is getting smaller due to the influence of wing geometry.

The momentum of the flow passing through the top surface must be heavier in order for more separation to occur with greater concentrate regions. The larger the separation area, the faster the stall. This has something to do with Figure 7 which shows the point where the stall occurs and Figure 9 where the focal area gets wider on the rectangular, elliptical, and semi-elliptical wings. In the Schuemann wing, even though the focus is getting wider, it is clustered in the direction of the leading edge and unlike other configurations, it is spreading to all sides of the upper surface.

### Wing geometry effect

The location of the stall point is closely related to the observed planform wing. The faster the stall point advances towards the leading edge, the faster the planform wing stalls. By using a rectangular wing as a comparison, all curved planform wings have negative pressure on the leading edge. However, the area

around the trailing edge experiences a different pattern of pressure areas. The Schuemann wing has the narrowest high-pressure pattern at the trailing edge.

The role of wing geometry is also very influential on the vorticity formation on the wing. The length of the wingtip greatly determines how long the vortex formation takes place. The longer the wingtip, the bigger the vortex. The wingtip length on the rectangular wing has the largest length so that the trailing edge has the largest vorticity area. On the other hand, the other planform wings have a smaller vorticity area because the wingtip length is smaller.

### Oswald's factor

Oswald's factor or Oswald's span efficiency factor are always used when discussing the relationship between wing span design and induced drag. This is greatly influenced by the wing planform and components attached to the wing. Oswald's efficiency factor was then transformed into several formulas that were adapted to the condition of the wing, for example with the addition of winglets by Asselin [27], straight wings and swept wings by Raymer [28], wings belonging to Douglas aircraft company by Shevell [2], and others.

Experts discuss more Oswald's factor on single and multi-engine aircraft than on UAVs. Therefore, the existing literature mentions more on high Re number than use on low Re for example in Gudmunsson [2], Kundu [29], and others. Some experts have discussed the low Re but limited to the flat plate wing as did Ananda et al. [30].

Given the limited information regarding the ratio of wing planforms at low Reynolds numbers, it is a great opportunity to research where the fixed-wing UAV velocity area is used. This study uses a speed of 10 m/s which is the minimum speed used by experts in UAV research, for example in the Kontogianis study [20]. In other fixed-wing UAVs, the speed used is slightly above that of Panagiotou's research [31]–[33], Turanoguz [34], and others. Research using the Eppler 562 airfoil has been carried out by Turanoguz [24], [34] using a speed of 45 m/s and Hariyadi [35]–[37] using a speed of 10 m/s. The resulting patterns of $C_D$, $C_L$, and $C_L/C_D$ are the same on the rectangular wing. The results of this study can pave the way for other researchers in exploring further research on planform wings at low Reynolds numbers.

## Conclusions

Numerical simulation on several planform wings found interesting phenomena to be investigated further. In this study, the Reynolds number used is the minimum average speed of the UAV so that it can be continued at a higher speed. From the numerical simulation carried out, we obtain the following conclusions, including:

i. The Schuemann wing produces the best performance that is indicated by the delaying of the stall point but also causes the largest induced drag. The result of total drag is mostly influenced by pressure drag and induced drag. However, the rectangular wing produces the best lift to drag ratio compared to other planform wings.
ii. The geometry of the wing affects the pressure contour and the location of the focus on the upper surface. With an increase in the angle of attack, the focus position is moving towards the mid-span due to the tip-vortex effect.
iii. With an increase in the angle of attack, the confluence of main flow and backflow is getting stronger, giving rise to a wider focus. This is evident from the change in the flow pattern on the upper surface at $\alpha = 12^o$ to $\alpha = 15^o$.
iv. The length of the wingtip affects how much area is affected by the presence of vortices on the trailing edge. The longer the wingtip, the wider the affected area.
v. When viewed from the stall point, the Schuemann wing has the angle of attack with the highest stall point. Meanwhile, when viewed from the overall aerodynamic performance, the rectangular wing is still better than all curved planform wings. However, this aerodynamic performance was observed at the minimum Reynolds number used by the UAV, so further research was carried out at a higher Reynolds number.

## Acknowledgement

This work was supported by Grant from Politeknik Penerbangan Surabaya.

## References

[1] C. Dole, *Flight theory and aerodynamics*, vol. 4, no. 3. 2017.
[2] Snorri Gudmundsson, *General Aviation Aircraft Design : Applied Methods*. 2013.
[3] Y. Azargoon, M. H. Djavareshkian, and E. Esmaeilifar, "Effect of airfoil distance to water surface on static stall," *Journal of Mechanical Engineering and Sciences*, vol. 14, no. 1, pp. 6526–6537, 2020.
[4] A. D. Gardner and K. Richter, "Influence of rotation on dynamic stall," *Journal of the American Helicopter Society*, vol. 58, no. 3, 2013.
[5] Q. Wang, Q. Zhao, and Q. Wu, "Aerodynamic shape optimization for alleviating dynamic stall characteristics of helicopter rotor airfoil," *Chinese Journal of Aeronautics*, vol. 28, no. 2, pp. 346–356, 2015.

[6] R. Pattermann, F. Sturm, and D. Benedikt, “On Stall Behavior in Aerobatic Figures with an Aerobatic Glider,” vol. 41, no. 2, pp. 16–25, 2017.
[7] A. Choudhry, R. Leknys, M. Arjomandi, and R. Kelso, “An insight into the dynamic stall lift characteristics,” *Experimental Thermal and Fluid Science*, vol. 58, pp. 188–208, 2014.
[8] R. R. Leknys, M. Arjomandi, R. M. Kelso, and C. Birzer, “Dynamic- and post-stall characteristics of pitching airfoils at extreme conditions,” *Proceedings of the Institution of Mechanical Engineers, Part G: Journal of Aerospace Engineering*, vol. 232, no. 6, pp. 1171–1185, 2018.
[9] M. R. Visbal and D. J. Garmann, “Effect of sweep on dynamic stall of a pitching finite-aspect-ratio wing,” *AIAA Journal*, vol. 57, no. 8, pp. 3274–3289, 2019.
[10] A. Medina, M. Rockwood, D. J. Garmann, and M. R. Visbal, “Integration of experiments and computations of swept-wing dynamic stall,” *AIAA Scitech 2019 Forum*, no. January, 2019.
[11] K. L. Tomek, A. H. Ullah, C. Fabijanic, and J. Estevadeordal, “Experimental investigation of dynamic stall on pitching swept finite-aspect-ratio wings,” *AIAA Scitech 2020 Forum*, vol. 1 PartF, no. January, pp. 1–35, 2020.
[12] J. H. Paterson, “Aerodynamic design features of the C-5A,” *SAE Technical Papers*, vol. 3, no. 6, 1967.
[13] P. Wang and Z. Shi, “Study of deep-stall characteristics and longitudinal special phenomena of T-tail aircraft,” *2010 IEEE International Conference on Mechatronics and Automation, ICMA 2010*, pp. 59–64, 2010.
[14] R. T. Taylor and E. J. Ray, “A Systematic Study of the Factors Contributing to Post-Stall Longitudinal Stability of T-Tail Transport Configurations,” in *AIAA Aircraft Design and Technology Meeting*, pp. 15–18, 1965.
[15] J. Winslow, H. Otsuka, B. Govindarajan, and I. Chopra, “Basic understanding of airfoil characteristics at low Reynolds numbers (104–105),” *Journal of Aircraft*, vol. 55, no. 3, pp. 1050–1061, 2018.
[16] M. Honarmand, M. H. Djavareshkian, B. F. Feshalami, and E. Esmaeilifar, “Numerical simulation of a pitching airfoil under dynamic stall of low Reynolds number flow,” *Journal of Aerospace Technology and Management*, vol. 11, no. 2010, pp. 1–14, 2019.
[17] J. D. Anderson and J. D. Anderson Jr, *Computational Fluid Dynamics The Basics with Applications*. 1995.
[18] F. R. Menter, “Two-equation eddy-viscosity turbulence models for engineering applications,” *AIAA Journal*, vol. 32, no. 8, pp. 1598–1605, 1994.
[19] S. A. Ahmadi, S. Sharif, and R. Jamshidi, “A numerical investigation on

the dynamic stall of a wind turbine section using different turbulent models," *World Academy of Science, Engineering and Technology*, vol. 58, pp. 290–296, 2009.

[20] S. G. Kontogiannis, D. E. Mazarakos, and V. Kostopoulos, "ATLAS IV wing aerodynamic design: From conceptual approach to detailed optimization," *Aerospace Science and Technology*, vol. 56, pp. 135–147, 2016.

[21] N. Mulvany, L. Chen, J. Tu, and B. Anderson, "Steady-State Evaluation of Two-Equation RANS (Reynolds-Averaged Navier-Stokes) Turbulence Models for High-Reynolds Number Hydrodynamic Flow Simulations," *Department of Defense, Australian Government*, pp. 1–54, 2004.

[22] E. Turanoguz and N. Alemdaroglu, "Design of a medium range tactical UAV and improvement of its performance by using winglets," *2015 International Conference on Unmanned Aircraft Systems, ICUAS 2015*, no. June 2015, pp. 1074–1083, 2015.

[23] S. P. Setyo Hariyadi, Sutardi, W. A. Widodo, and M. A. Mustaghfirin, "Aerodynamics analysis of the wingtip fence effect on UAV wing," *International Review of Mechanical Engineering*, vol. 12, no. 10, 2018.

[24] E. Turanoguz, "Design of a Medium Range Tactical," no. September, 2014.

[25] S. P. Setyo Hariyadi, Sutardi, and W. A. Widodo, "Numerical study of flow characteristics around wing airfoil Eppler 562 with variations of rearward wingtip fence," in *AIP Conference Proceedings*, vol. 1983, 2018.

[26] S. S. P. Hariyadi, Sutardi, and W. A. Widodo, "Drag reduction analysis of wing airfoil E562 with forward wingtip fence at cant angle variations of 75°and 90°," in *AIP Conference Proceedings*, vol. 2001, 2018.

[27] M. Asselin, "An Introduction to Aircraft Performance," *An Introduction to Aircraft Performance*, 1997.

[28] Raymer, "D. Raymer - Aircraft Design. A Conceptual Approach (1992).pdf." p. 745, 1992.

[29] A. K. Kundu, M. A. Price, and D. Riordan, *Conceptual Aircraft Design: An Industrial Approach*. 2019.

[30] G. K. Ananda, P. P. Sukumar, and M. S. Selig, "Measured aerodynamic characteristics of wings at low Reynolds numbers," *Aerospace Science and Technology*, vol. 42, pp. 392–406, 2015.

[31] P. Panagiotou, P. Kaparos, and K. Yakinthos, "Winglet design and optimization for a MALE UAV using CFD," *Aerospace Science and Technology*, vol. 39, pp. 190–205, 2014.

[32] P. Panagiotou and K. Yakinthos, "Aerodynamic efficiency and performance enhancement of fixed-wing UAVs," *Aerospace Science and Technology*, vol. 1, pp. 105575, 2019.

[33] P. Panagiotou, C. Salpingidou, P. Kaparos, and K. Yakinthos, "A CFD-

Aided Design Procedure, Performance Estimation and Optimization Study of a Male Uav," no. July, 2015.

[34] E. Turanoguz and N. Alemdaroglu, "Design of a medium range tactical UAV and improvement of its performance by using winglets," *2015 International Conference on Unmanned Aircraft Systems, ICUAS 2015*, no. June 2015, pp. 1074–1083, 2015.

[35] S. P. Setyo Hariyadi, Sutardi, W. A. Widodo, and M. A. Mustaghfirin, "Aerodynamics analysis of the wingtip fence effect on UAV wing," *International Review of Mechanical Engineering*, vol. 12, no. 10, pp. 837–846, 2018.

[36] S. P. Setyo Hariyadi, Sutardi, and W. A. Widodo, "Numerical study of flow characteristics around wing airfoil Eppler 562 with variations of rearward wingtip fence," *AIP Conference Proceedings*, vol. 1983, 2018.

[37] S. S. P. Hariyadi, Sutardi, and W. A. Widodo, "Drag reduction analysis of wing airfoil E562 with forward wingtip fence at cant angle variations of 75°and 90°," *AIP Conference Proceedings*, vol. 2001, 2018.